Eur. Phys. J. A (2012) **48**: 191
DOI 10.1140/epja/i2012-12191-5

THE EUROPEAN PHYSICAL JOURNAL A

Regular Article – Experimental Physics

One-neutron knockout from $^{51-55}$Sc

S. Schwertel[1], P. Maierbeck[1], R. Krücken[1,2,3,a], R. Gernhäuser[1], T. Kröll[1,4], H. Alvarez-Pol[5], F. Aksouh[6], T. Aumann[6], K. Behr[6], E.A. Benjamim[5], J. Benlliure[5], V. Bildstein[1], M. Böhmer[1], K. Boretzky[6], M.J.G. Borge[7], A. Brünle[6], A. Bürger[8,9], M. Caamaño[5], E. Casarejos[10], A. Chatillon[6], L.V. Chulkov[6], D. Cortina-Gil[5], J. Enders[4], K. Eppinger[1], T. Faestermann[1], J. Friese[1], L. Fabbietti[1], M. Gascón[5], H. Geissel[6], J. Gerl[6], M. Gorska[6], P.G. Hansen[11,†], B. Jonson[12], R. Kanungo[13,2,6], O. Kiselev[6,14,15], I. Kojouharov[6], A. Klimkiewicz[6], T. Kurtukian[5], N. Kurz[6], K. Larsson[6,12], T. Le Bleis[6,16], K. Mahata[6,15], L. Maier[1], T. Nilsson[12,4], C. Nociforo[6], G. Nyman[12], C. Pascual-Izarra[7], A. Perea[7], D. Perez[5], A. Prochazka[6,18], C. Rodriguez-Tajes[5], D. Rossi[14], H. Schaffner[6], G. Schrieder[4], H. Simon[6], B. Sitar[18], M. Stanoiu[6], K. Sümmerer[6], O. Tengblad[7], H. Weick[6], S. Winkler[1], B.A. Brown[10], T. Otsuka[19], J.A. Tostevin[20], and W.D.M. Rae[21]

[1] Physik Department E12, Technische Universität München, 85748 Garching, Germany
[2] TRIUMF, 4004 Wesbrook Mall, Vancouver, B.C. V6T 2A3, Canada
[3] Department of Physics & Astronomy, University of British Columbia, Vancouver, B.C. V6T 1Z1, Canada
[4] Institut für Kernphysik, Technische Universität Darmstadt, 64289 Darmstadt, Germany
[5] Departamento de Física de Partículas, Universidade de Santiago de Compostela, 15782 Santiago de Compostela, Spain
[6] GSI Helmholtzzentrum für Schwerionenforschung, 64291 Darmstadt, Germany
[7] Instituto de Estructura de la Materia, CSIC, 28006 Madrid, Spain
[8] SAFE/OCL, University of Oslo, N-0316 Oslo, Norway
[9] CEA, Saclay, DSM/IRFU/SPhN, F-91191 Gif-sur-Yvette, France
[10] University of Vigo, E-36310, Spain
[11] NSCL, Michigan State University, East Lansing, Michigan 48824, USA
[12] Experimentell Fysik, Chalmers Tekniska Högskola och Göteborgs Universitet, 412 96 Göteborg, Sweden
[13] Saint Mary's University, 923 Robie St., Halifax, Nova Scotia B3H 3C3, Canada
[14] Johannes Gutenberg Universität, 55099 Mainz, Germany
[15] Paul Scherrer Institut, 5232 Villigen, Switzerland
[16] Institut Pluridisciplinaire Hubert Curien IN2P3-CNRS/Université Louis Pasteur, F-67037 Strasbourg Cedex 2, France
[17] Nuclear Physics Division, Bhabha Atomic Research Centre, Mumbai, 400 085, India
[18] Faculty of Mathematics and Physics, Comenius University, 84215 Bratislava, Slovakia
[19] Department of Physics, University of Tokyo, Hongo, Bunkyo-ku, Tokyo, 113-0033, Japan
[20] Department of Physics, Faculty of Engineering and Physical Sciences, University of Surrey, Guildford, Surrey GU2 7XH, UK
[21] Garsington, Oxfordshire, OX44, UK

Received: 9 October 2012 / Revised: 5 November 2012
Published online: 20 December 2012 –
Communicated by J. Äystö

Abstract. Results are presented from a one-neutron knockout experiment at relativistic energies of ≈ 420 A MeV on $^{51-55}$Sc using the GSI Fragment Separator as a two-stage magnetic spectrometer and the MINIBALL array for gamma-ray detection. Inclusive longitudinal momentum distributions and cross-sections were measured enabling the determination of the contributions corresponding to knockout from the $\nu p_{1/2}$, $\nu p_{3/2}$, ($L = 1$) and $\nu f_{7/2}$, $\nu f_{5/2}$ ($L = 3$) neutron orbitals. The observed $L = 1$ and $L = 3$ contributions are compared with theoretical cross-sections using eikonal knockout theory and spectroscopic factors from shell model calculations using the GXPF1A interaction. The measured inclusive knockout cross-sections generally follow the trends expected theoretically and given by the spectroscopic strength predicted from the shell model calculations. However, the deduced $L = 1$ cross-sections are generally 30–40% higher while the $L = 3$ contributions are about a factor of two smaller than predicted. This points to a promotion of neutrons from the $\nu f_{7/2}$ to the $\nu p_{3/2}$ orbital indicating a weakening of the $N = 28$ shell gap in these nuclei. While this is not predicted for the phenomenological GXPF1A interaction such a weakening is predicted by recent calculations using realistic low-momentum interactions $V_{low k}$ obtained by evolving a chiral N3LO nucleon-nucleon potential.

[a] e-mail: reiner.kruecken@triumf.ca
[†] Deceased.

1 Introduction

The modification of shell structure in neutron-rich nuclei is at the center of a number of current experimental and theoretical studies (see refs. [1,2] for recent reviews). In particular the evolution of effective single-particle energies due to the monopole component of the tensor interaction has been found to be an important driver of shell modifications [3–5]. More recently the role of three-body forces has been discussed [6] as contributing substantially to the shell modifications leading to the new doubly magic nucleus ^{24}O [7,8]. Shell model calculations for the pf-shell with a phenomenological interaction that includes these effects (GXPF1,GXPF1A) [9–11] predict a new neutron shell closure at $N = 34$ for the Ca isotopes. However, this prediction remains controversial since shell model calculations with the KB3G interaction [12–15] and the related UPF interaction [16] as well as beyond-mean-field calculations [17] support the well-established $N = 32$ $\nu p_{3/2}$ sub-shell closure but not a sizable $N = 34$ gap.

While it has not been possible so far to directly investigate the structure of ^{54}Ca itself, there has been significant activity on studying the nuclei in its direct vicinity [16, 18–32]. However, the picture that has emerged from this experimental information is not completely clear regarding the existence of the $N = 34$ shell closure in ^{54}Ca and more data are clearly needed. In addition, recent calculations using realistic low-momentum interactions V_{lowk} obtained by evolving a chiral N3LO nucleon-nucleon (NN) potential [33] indicate a substantially different evolution of single-particle energies in the Ca isotopes relative to phenomenological interactions such as GXPF1A. These calculations attribute the origin of the $N = 34$ shell gap to effects of three-nucleon forces. At the same time these calculations show that the use of realistic interactions leads consistently to a lowering of the $\nu p_{3/2}$ orbital between $N = 28$ and $N = 34$, effectively eliminating the $N = 28$ shell gap in ^{54}Ca. These calculations also show good agreement with neutron separation energies deduced from most recent mass measurements of neutron-rich Ca isotopes up to ^{52}Ca [34].

In this context the investigation of the evolution of the active neutron single-particle orbitals in the odd-Z Sc isotopes may add important additional information. Knowledge on excited states in the neutron-rich Sc isotopes $^{51-54}$Sc was recently substantially extended [16,26, 30]. In the present paper we report on results from the one-neutron knockout at relativistic energies from the scandium isotopes $^{51-55}$Sc. Results on ^{55}Ti from the same experiment were already reported in [32] and showed good agreement with shell model predictions obtained with the GXPF1A interaction for a $1/2^-$ ground state in ^{55}Ti. Here we report on inclusive knockout cross-sections and momentum distributions from which the contributions of $L = 1$ and $L = 3$ knockout from neutrons in the pf-shell orbitals were extracted. The results are compared with theoretical nucleon-removal reaction cross-sections using spectroscopic factors from shell model calculations.

2 Experimental setup

The experiment was performed at the *GSI Helmholtzzentrum für Schwerionenforschung* at Darmstadt (Germany). The UNILAC and SIS accelerator complex provided a 500 A MeV ^{86}Kr primary beam with an intensity of up to 10^9 particles per second. The secondary beams of $^{51-55}$Sc were produced in a fragmentation reaction in a ^{9}Be target (1625 mg/cm^2) positioned in front of the GSI fragment separator (FRS) [35]. The four 30° magnetic dipoles of the separator were used as a two-stage spectrometer. The primary fragments of interest ($^A_{21}$Sc$_N$) were identified in the first separator stage on an event-by-event basis. The secondary ^{9}Be target (1720 mg/cm^2) for the knockout reaction was placed at the middle focal plane (F2) of the FRS. The reaction energy of the primary fragments in the middle of the secondary target was $\approx$ 420 A MeV. The second FRS stage was used for the identification of the $^{A-1}_{21}$Sc$_{N-1}$ residual nuclei.

Figure 1 schematically shows the FRS set-up and the detector assemblies at the different focal planes of the FRS. Scintillation counters (Sci) at F1, F2, and F4 were used to measure the time-of-flight (TOF) from F1 to F2 and F2 to F4, respectively, and thus the velocity $\beta = v/c$ of the fragments. Multi sampling ionization chambers (MUSIC) at F2, before the secondary target, and at F4 were used for energy loss measurements of the fragments from which the nuclear charge Z of the fragments was determined.

The position of the fragments was measured with six time projection chambers (TPC) [36], two each in front and after the knockout target at the middle focal plane (F2) of the FRS and the last two at the final focus (F4). The magnetic rigidity $B\rho$ of each fully stripped fragment (atomic charge q = nuclear charge Z) was determined from the measured position and the known magnetic fields of the FRS magnets.

The momentum of the particle,

$$p = \beta\gamma \cdot A \cdot m_0 = B\rho \cdot q,$$

and the mass-to-charge ratio,

$$\frac{A}{q} = \frac{B\rho}{\beta\gamma \cdot m_0},$$

were determined from the measured quantities on an event-by-event basis. Here $\gamma = 1/\sqrt{1-\beta^2}$ and $m_0 = 931.5\,\mathrm{MeV}/c^2$.

The detector systems were calibrated using a primary ^{48}Ca beam. For the isotopes of interest a mass and charge resolution of $\Delta A = 0.28$ and $\Delta Z = 0.22$ were measured, respectively. The identification of the incoming and outgoing fragments at the knockout target allowed the selection of the reaction of interest (see fig. 2).

The TPC pairs were separated by 1690 mm (before the knockout target), 920 mm (after the knockout target) and 1490 mm at F4, respectively, providing the measurement of incident and emergent angles of the fragments at F2 and F4. This enabled the reconstruction of the flight path

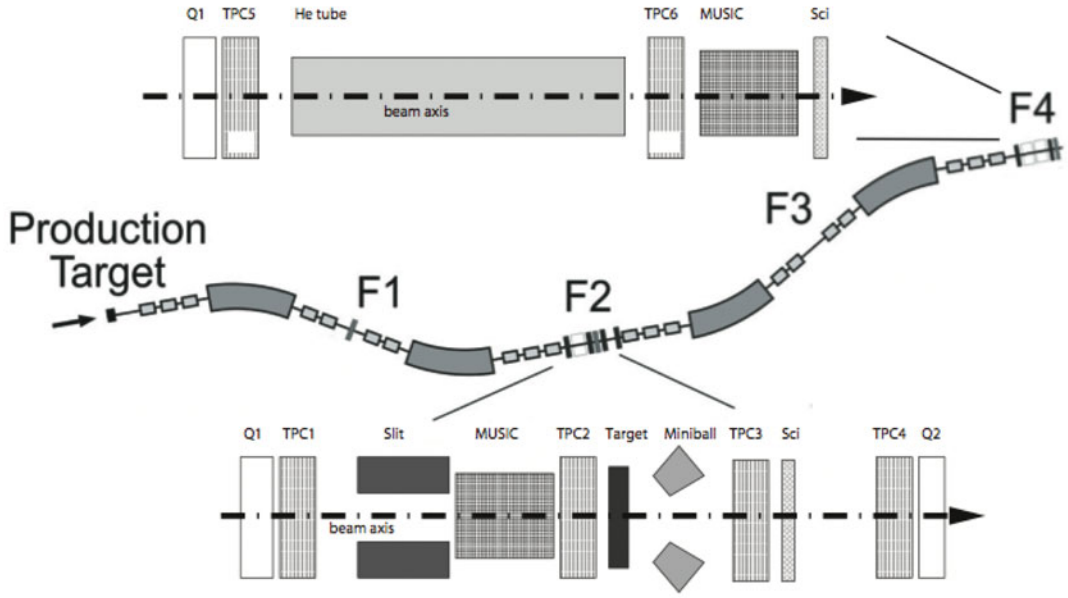

Fig. 1. Sketch of the FRS and the detector systems at the focal planes F2 and F4.

within the FRS. The two stages of the FRS were operated in a dispersion matched mode with a chromatic focus at F2 and an achromatic focus at F4. With this mode both the momentum of the incoming and the outgoing fragment could be measured and therefore the momentum transfer induced by the reaction could be determined. A detailed description of the method of momentum analysis will be given in sect. 4.

Gamma rays emitted from excited states populated in the knockout reaction were measured by the eight clusters of the MINIBALL spectrometer [37]. Each cluster contains three six-fold segmented high-purity germanium (HPGe) crystals. All clusters were mounted downstream of the target at a central angle of 40° with respect to the beam axis and a distance of about 290 mm from the center of the target to the front of the HPGe crystals. The azimuthal angle between neighboring cluster centers was 45°. This arrangement takes advantage of the Lorentz boost of the solid angle in the forward direction. Using the segmentation of the detectors an improved Doppler correction could be performed for the fast moving residual nuclei ($\beta = 0.7$), leading to a FWHM resolution of 40 keV for gamma-ray energies of $\approx$ 580 keV in the c.m. system of the emitting nucleus. By tagging on a transition in the gamma-ray spectrum, the population of excited states in the residual nuclei can be selected, which allows for the exclusive measurement of the momentum distribution associated with this state. This was used in the case of ^{52}Sc, which will be discussed later on.

3 Cross-section measurement

For the determination of the knockout cross-section the number of reactions within the target has to be measured, which is related to the ratio of the number of residual reaction products to the number of incoming primary fragments at the knockout target.

In order to determine the rate of incoming primary fragments and the number of produced reaction products two triggers were used in the data acquisition (DAQ) system. For the incoming primary fragments a downscaled trigger signal was derived from the F2 scintillator before the knockout target. Downscaling was necessary in order to limit the dead time of the DAQ and scaling factors of 2^N with $N = 5$–8 for different runs were used in the experiment. The main trigger of the DAQ was derived from a coincidence between the F2 and F4 scintillators, thus tagging on knockout reaction products identified at F4. Rate dependent dead time corrections of both trigger efficiencies could be performed on the basis of the measured data.

To calculate the cross-section, the number of detected incoming and outgoing particles have to be corrected for losses during the transport of the beam and/or reaction products from F2 to F4, misidentification of fragments at F4, or disintegration of the reaction products by secondary reactions in the beam-line detectors. One can make the reasonable assumption that the primary ${}^{A}_{21}\mathrm{Sc}_N$ fragment and the ${}^{A-1}_{21}\mathrm{Sc}_{N-1}$ reaction product have a comparable identification probability, destruction rate, and optical transmission between F2 and F4. Therefore, these correction factors can be determined by a separate measurement with identified ${}^{A}_{21}\mathrm{Sc}_N$ nuclei at both focal planes. The transmission, the ratio of identified identical nuclei at the two focal planes, includes all the aforementioned corrections. It also considers the destruction of incoming particles and outgoing reaction products, respectively, in the knockout target. The transmission can be determined directly from the data. However, especially for the knockout

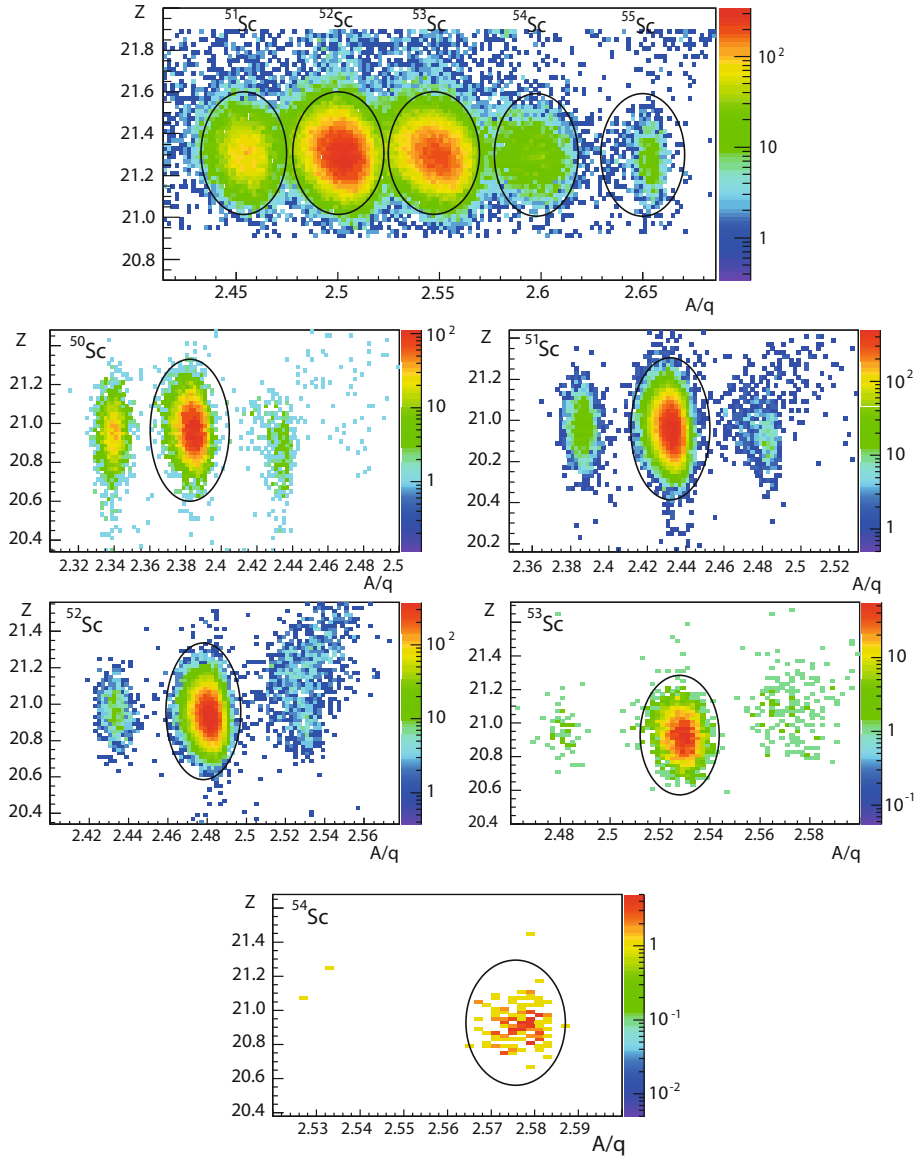

Fig. 2. (Color online) Identification of the fragments at F2 and F4. The upper panel shows $^{51-55}$Sc primary fragments at the middle focus F2 of the FRS. The pictures beneath show the respective PID plots at F4 gating on one isotope at F2. The black ellipses indicate the one-neutron knockout product.

reactions ^{54}Sc→^{53}Sc and ^{55}Sc→^{54}Sc the limited statistics leads to quite large uncertainty (up to ≈ 60%). To address this issue, the transmission was also calculated with the simulation code MOCADI [38] for all $^{A}\mathrm{Sc}_N \rightarrow {}^{A-1}\mathrm{Sc}_{N-1}$ reactions. For the reactions with better statistics the simulations agree well with the experimental results within the uncertainties of about 15–19% which gives confidence that the simulations are reliable. Therefore, the calculated transmissions were used for all further discussions.

Another correction to be considered results from the fact that knockout reactions can occur not only in the target but also in matter outside of the target. Since it is impossible to distinguish such reactions directly, an empty target measurement with a corresponding transmission correction was performed to determine the number of reactions outside the target.

The difference between the measurements with and without target leads to the probability P_{KO} of a knockout reaction in the target. Using the thickness of the target ($\mu = 1720\,\mathrm{mg/cm^2}$), Avogadro's constant ($N_A = 6.022 \cdot 10^{23}\,\mathrm{mol^{-1}}$) and the molar mass of beryllium ($m_{mol} = 9.012\,\mathrm{g/mol}$) one obtains the single-nucleon knockout cross-section σ_{KO}

$$\sigma_{KO} = \frac{P_{KO}}{\mu \frac{N_A}{m_{mol}}} = P_{KO} \cdot 8.70(4)\,\mathrm{b}. \quad (1)$$

The systematic error results from the uncertainty of the thickness of the ^{9}Be target of smaller than 5‰, determined in a thickness scan with a mesh of 200 points. In comparison to the statistical errors of the measurements (see sect. 5), this error will be neglected in the further discussion.

4 Momentum distribution measurement

In addition to the cross-section, the longitudinal momentum distribution of the residual nucleus is another important observable in the knockout reaction. In the dispersion matched mode (see sect. 2) with no momentum transfer at F2 the residual nucleus is focused onto the F4 focal plane, independent of emergent angle and momentum at F2. Any change of momentum due to the reaction, parallel to the direction of motion, leads to a displacement at the final focus and thus can be detected. Since the absolute momentum is measured at F2 and F4, the parallel momentum transfer in the reaction can be determined.

The momentum p of a $^{A-1}\mathrm{Sc}_{N-1}$ nucleus after the reaction target is calculated using [39]

$$p = p_{F2} - \frac{x_4 - x_2 \cdot (M_{24} + \delta \frac{D_{24}}{D_{02}} \frac{p_2}{p_4})}{D_{24}} \cdot p_{F4}, \qquad (2)$$

with the following parameters.

- x_2: horizontal position at F2.
- x_4: horizontal position at F4.
- p_{F2}: measured momentum at F2.
- p_2: nominal momentum at F2.
- p_4: nominal momentum at F4.
- D_{02}: dispersion FRS production target → F2.
- D_{24}: dispersion F2 → F4.
- M_{24}: magnification factor F2 → F4.
- δ: compensation for energy loss at F2.

The dispersions and the magnification factor were obtained in separate measurements with a 452 A MeV primary ^{48}Ca beam to be $D_{02} = -4.49\,\mathrm{cm/\%}$, $D_{24} = 8.03\,\mathrm{cm/\%}$, and $M_{24} = 1.72$, respectively. The magnification factor thus compensates for the difference between the two dispersions. Due to the dispersion, the position at the middle focal plane depends on the momentum of the nucleus in the magnetic fields of the first stage of the FRS. For the calculation of the momentum transfer in the reaction the momentum in the middle of the reaction target is needed. For this it is important to take into account the different energy loss for particles with different momenta, which is different for different positions at F2. This effect is compensated by the correction factor δ [39], which is empirically determined for each knockout reaction $^{A}\mathrm{Sc}\rightarrow{}^{A-1}\mathrm{Sc}$ such that the resulting momentum distribution shows no dependence on the position at F2.

With the procedure described above, a laboratory frame momentum distribution could be obtained for each knockout reaction. Similar to the cross-section analysis, a correction for knockout reactions in matter other than the target has to be performed. Since without the target there is no energy loss of the beam, the magnetic settings for the second stage of the FRS differed between the measurement with and without target. The scaling of the magnets were calculated for ^{56}Ti ($Z = 22$), which was the main focus of this experiment [32]. The left part of fig. 3 shows the position distribution at F4 for the transmission measurements for ^{56}Ti with (upper panel) and without (lower panel) reaction target. Within the statistical uncertainties, there is no deviation in the measured position. In this case, the momentum distributions for reactions inside and outside the target obtained from eq. (2) can simply be subtracted from each other after appropriate scaling according to the measured cross-sections for either case.

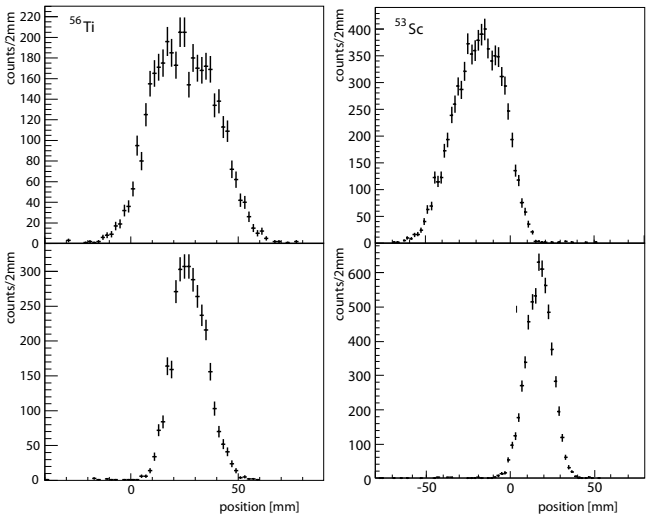

Fig. 3. Left: Position distribution at the final focus F4 of ^{56}Ti, with (upper row) and without (lower row) reaction target at F2. The scaling of the magnets compensates the missing energy loss without target, so the mean of the distributions match. The error bars represent statistical uncertainties only. Right: Same for ^{53}Sc where a significant shift is observed in the position between the measurements with and without target and a correction has to be applied to the data (see text for details).

Table 1. Position corrections at F4 for the different ^{A}Sc isotopes.

Nucleus at F2	Correction [mm]
^{51}Sc	−17.7
^{52}Sc	−23.4
^{53}Sc	−35.9
^{54}Sc	−45.2
^{55}Sc	−52.9

In contrast, for Sc isotopes ($Z = 21$) the difference in energy loss at F2 is not compensated correctly by the scaling of the magnets. This leads to a displacement of the position distributions at the final focus for measurements with and without the knockout target at F2, respectively. As an example, the right part of fig. 3 shows the position distribution at F4 for the ^{53}Sc transmission measurements with (upper panel) and without (lower panel) the reaction target. Due to this shift a correction of the position distribution at the final focus is needed to calculate the momentum distribution with eq. (2). The correction can be deduced by determining the difference of the mean values of the position distributions of the respective transmission measurements for each ^{A}Sc nucleus. The correction values are listed in table 1. Using this correction for the empty target measurement, the momentum distribution of the

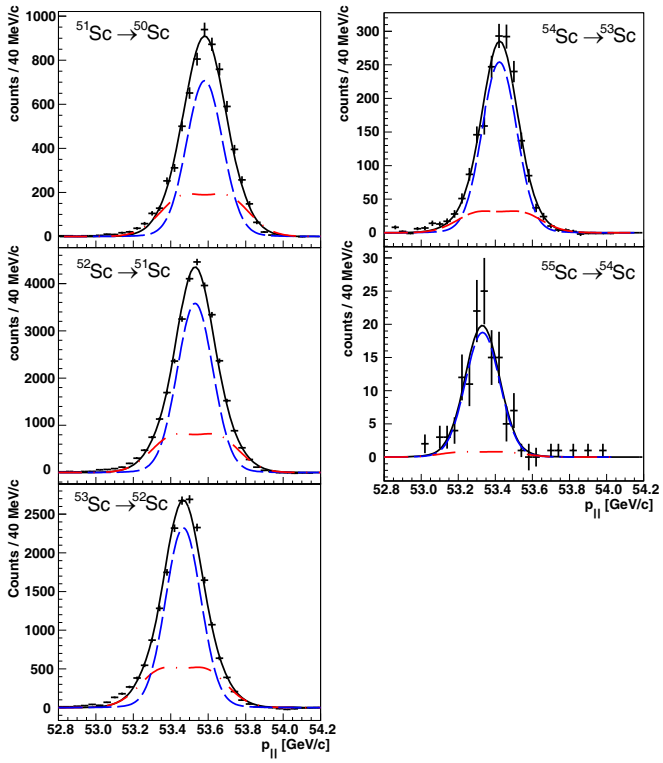

Fig. 4. (Color online) Measured longitudinal momentum distributions of all observed reactions and total fitted momentum distributions (solid line) with $L = 1$ (blue, dashed) and $L = 3$ (red, dash-dotted) contributions.

residual nuclei after knockout reactions in the target at F2 can be obtained by subtracting the distributions measured with and without target from each other. The empty target measurement also allowed for a measurement of the momentum resolution of the setup, for which a FWHM of 150 MeV/c was obtained, corresponding to a relative momentum resolution of $2.7 \cdot 10^{-3}$.

5 Results

In this experiment we measured longitudinal momentum distributions and inclusive cross-sections for the one-neutron-knockout reactions $^{51-55}$Sc → $^{50-54}$Sc.

The shape of the momentum distribution for the knockout of a nucleon from a certain single-particle orbital is characteristic of the orbital angular momentum L of this orbital. It is advantageous to measure the longitudinal component of the momentum distribution because it is less affected by diffractive scattering and Coulomb deflection, which are both transverse for forward-focused reactions [40].

The measured longitudinal momentum distributions for the knockout reactions $^{51-55}$Sc → $^{50-54}$Sc are shown in fig. 4. These experimental distributions are compared to theoretical momentum distributions for the removal of a neutron from the pf-shell that were calculated following the procedure outlined below (see also [32]).

Table 2. Measured (left) and calculated (right) cross-sections for the one-neutron knockout from $^{51-55}$Sc. Inclusive cross-sections as well as the contributions from $L = 1$ and $L = 3$ knockout are listed. For the theoretical cross-sections all contributing shell model states below the neutron separation energy S_n are taken into account.

	Cross-section [mb]					
	Experiment			Theory		
	Σ	$L = 1$	$L = 3$	Σ	$L = 1$	$L = 3$
^{51}Sc	78(16)	54(16)	24(10)	101	27	74
^{52}Sc	98(15)	66(10)	32(5)	113	42	71
^{53}Sc	102(15)	68(10)	34(5)	130	59	71
^{54}Sc	113(17)	91(14)	22(5)	87	65	22
^{55}Sc	72(14)	69(16)	3(9)	99	93	6

The relative contributions of $L = 1$ and $L = 3$ knockout were determined by fitting the experimental momentum distributions with the weighted sum of theoretical $L = 1$ and $L = 3$ momentum distributions, after folding them with the instrumental resolution. Figure 4 shows the best fit to the experimental momentum distributions as a solid line as well as the fitted $L = 1$ (blue, dashed) and $L = 3$ (red, dash-dotted) contributions for each knockout residue. Overall there is very good agreement between the experimental data and the fits.

Experimental values for the inclusive cross-sections were determined as outlined in sect. 3 and are tabulated in table 2. On the basis of the relative contributions of the $L = 1$ and $L = 3$ knockout to the momentum distributions the cross-sections for removal of a neutron from the $\nu f_{7/2}$, $\nu f_{5/2}$ and the $\nu p_{3/2}$, $\nu p_{1/2}$ orbitals could be determined, which are also listed in table 2.

The cross-sections determined for $L = 1$ and $L = 3$ knockout in $^{51-55}$Sc can be compared to theoretical predictions. Towards this aim theoretical single-neutron removal cross-sections were computed for the $\nu f_{7/2}$, $\nu p_{3/2}$, $\nu p_{1/2}$, and $\nu f_{5/2}$ orbitals. For the theoretical single-nucleon removal cross-sections contributions from both the stripping mechanism (with excitation of the target by the removed nucleon) and the diffractive breakup mechanism have been considered. These contributions are computed from the residue- and nucleon-target eikonal S-matrices via the optical limit of Glauber theory following ref. [40]. The elastic S-matrices were calculated using the point proton and neutron densities of the residues, taken from Skyrme (SkX) Hartree-Fock (HF) calculations [41]. The ^{9}Be density was assumed to be a Gaussian with a root mean squared (rms) radius of 2.36 fm. A zero-range forward scattering nucleon-nucleon (NN) amplitude was assumed with real-to-imaginary ratios interpolated from the table of Ray [42]. The rms radii of the removed nucleons' single-particle wave functions were also constrained by Skyrme (SkX) HF calculations (see ref. [43] for details). A fixed diffuseness parameter $a_0 = 0.7$ fm and a spin-orbit interaction of 6 MeV were used for all cases.

Table 3. Neutron separation energies S_n in the residual nuclei taken from the 2011 mass evaluation (AME2011) [45].

	S_n [MeV]
^{50}Sc	6.057(15)
^{51}Sc	6.753(25)
^{52}Sc	5.200 (194)
^{53}Sc	5.254(355)
^{54}Sc	4.206(585)

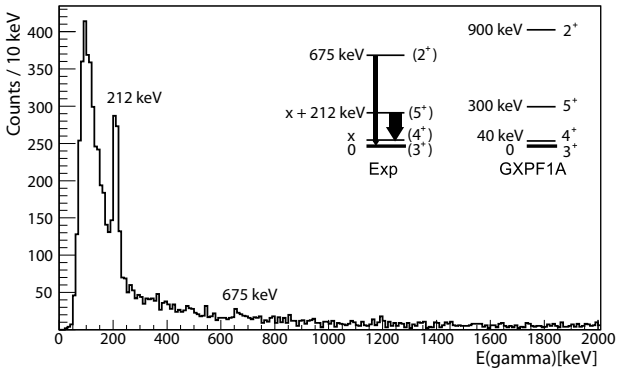

Fig. 5. Doppler corrected γ-ray energy spectrum for ^{52}Sc. The insert shows the level scheme as it was derived from [16].

To compare with experiment the single-particle cross-sections, calculated for unit spectroscopic strength, were multiplied by the shell model spectroscopic factors, which in the present case were calculated using a ^{40}Ca core and the GXPF1A residual interaction [10,11]. In these calculations the spectroscopic factors for removal of a p- and f-state neutron were taken into account for levels up to energies of about 7 MeV in the residual nuclei. Table 2 lists the sum of the $L = 1$ and $L = 3$ knockout cross-sections for all states up to the neutron separation energy in the residual $^{50-54}$Sc nuclei (see table 3), respectively, which is the value that can be compared to the measured cross-sections. Since the ground-state spins of ^{52}Sc and ^{54}Sc could be 3^+ or 4^+ calculations for both assumptions have been performed. The resulting cross-sections do not differ significantly. Therefore, we show for simplicity only the results for the 4^+ assumption.

In addition to the measurement of inclusive cross-sections it was possible to observe individual excited states in some of the residual nuclei. No new transitions were observed in our study. Only in the ^{53}Sc→^{52}Sc reaction were the statistics sufficient to extract a momentum distribution in coincidence with the depopulating gamma-ray transitions in ^{52}Sc. Figure 5 shows the Doppler corrected gamma-ray spectrum for ^{52}Sc. While the 212 keV transition is very prominent only a hint of the 675 keV transition is visible. Both transitions were previously observed [16, 26] and the insert of fig. 5 indicates their placement in the level scheme of ^{52}Sc.

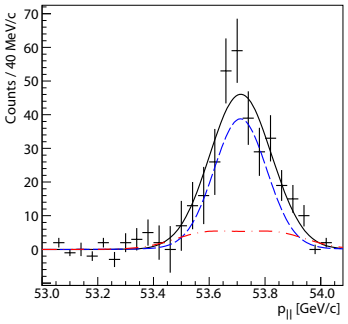

Fig. 6. (Color online) Background subtracted longitudinal momentum distribution in coincidence with the 212 keV gamma-ray transition in ^{52}Sc. The solid line is a fit composed of a $L = 1$ and $L = 3$ contribution. The red dash-dotted (blue dashed) line is the $L = 3$ ($L = 1$) component contributing to the fit.

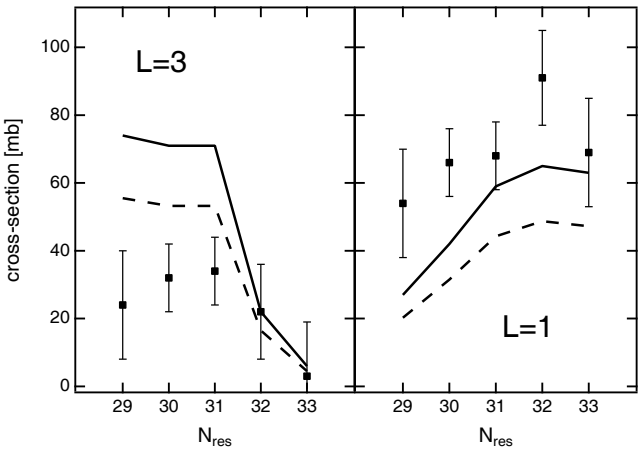

Fig. 7. Comparison of experimental (squares) and theoretical knockout cross-sections for $L = 3$ (left) and $L = 1$ (right) as a function of neutron number of the knockout residue. The theoretical cross-sections are shown for the full spectroscopic factors from the SM calculations (solid line) and spectroscopic factors reduced by a factor 0.75 (dashed line).

Figure 6 shows the longitudinal momentum distribution in coincidence withe the 212 keV transition following background subtraction. Clearly, the $L = 1$ contribution dominates, as one would expect due to the assigned $\pi f_{7/2} \times \nu p^3_{3/2}$ character of both observed states [16,26], resulting from the knockout of one $\nu p_{3/2}$ neutron in ^{53}Sc.

6 Discussion

The experimentally determined and the theoretically predicted cross-sections for $L = 1$ and $L = 3$ knockout are shown in fig. 7 as a function of neutron number N_{res} of the residual nucleus detected at the FRS focal plane. By taking the ratio of measured cross-sections to the theoretical single-neutron removal cross-sections experimental spectroscopic factors were determined for the $L = 1$ and

Table 4. Experimental and theoretically determined spectroscopic factors for $L = 1$ and $L = 3$ orbitals for the investigated knockout reactions. For the theoretical SF values, which were calculated with the GXPF1A interaction, the strengths of all states below the neutron separation energy in the residual nucleus was summed. These spectroscopic factors can be interpreted as the occupation of the respective orbtials in the initial nucleus.

Reaction	SF_{exp}		SF_{th}			
	$L = 1$	$L = 3$	$\nu p_{3/2}$	$\nu p_{1/2}$	$\nu f_{7/2}$	$\nu f_{5/2}$
^{51}Sc $\rightarrow$ ^{50}Sc	3.9(6)	2.4(4)	1.78	0.16	7.32	0.10
^{52}Sc $\rightarrow$ ^{51}Sc	4.5(7)	3.5(5)	2.71	0.15	7.17	0.08
^{53}Sc $\rightarrow$ ^{52}Sc	4.4(6)	3.5(5)	3.46	0.32	7.13	0.12
^{54}Sc $\rightarrow$ ^{53}Sc	6.7(10)	3.1(7)	3.67	1.00	2.87	0.07
^{55}Sc $\rightarrow$ ^{54}Sc	4.1(9)	0.3(9)	3.62	1.86	0.44	0.13

$L = 3$ contributions, respectively. These values are listed in table 4 (for the initial nuclei) together with the sums of spectroscopic factors calculated within the SM for the $\nu p_{3/2}$ and $\nu p_{1/2}$ ($L = 1$) as well as the $\nu f_{7/2}$ and $\nu f_{5/2}$ ($L = 3$) orbitals for all states below the neutron separation energy in the residual nucleus. From the theoretical spectroscopic factors of the individual orbitals one can nicely see the successive occupation of the single-particle levels. For the $\nu f_{7/2}$ the summed spectroscopic factors for the reactions ^{54}Sc$\rightarrow$^{53}Sc and ^{55}Sc$\rightarrow$^{54}Sc are 7.08 and 7.24, respectively, when all levels in the residual nucleus are taken into account, including those above the neutron separation energy. It is also clear from these values that the $\nu f_{5/2}$ is not contributing significantly because of the $N = 34$ gap in the GXPF1A SM calculations.

Before experimental and theoretical values are compared more closely, one should take note of the origin of the trends displayed by the theoretical values. In the SM calculations using the GXPF1A interaction the $\nu f_{7/2}$ orbital is basically fully occupied in $^{51-55}$Sc while with increasing neutron number successively more neutrons are placed into the $\nu p_{3/2}$ and $\nu p_{1/2}$ orbitals. This leads to the almost linear rise of the calculated cross-sections for $L = 1$ knockout. Since the $\nu f_{5/2}$ orbital is well above the $\nu p_{1/2}$ orbital in the GXPF1A calculations the $\nu f_{5/2}$ orbital is basically not occupied for $^{51-55}$Sc and thus does not contribute to the $L = 3$ knockout cross-section. The flat $L = 3$ cross-section for $N_{res} = 29$–31 reflects the constant contribution from the fully occupied $\nu f_{7/2}$ orbital. The drop of the theoretical $L = 3$ cross-section at $N_{res} = 32$ is simply due to the fact that with increasing neutron number the $\nu f_{7/2}$ strength is shifted to higher excitation energies and for $N_{res} = 32, 33$ is situated almost completely above the neutron separation energy. This is demonstrated in fig. 8 where the distribution of the calculated spectroscopic factors for the reactions ^{53}Sc$\rightarrow$^{52}Sc and ^{55}Sc$\rightarrow$^{54}Sc are shown as function of the excitation energy in the residual nucleus. One can see the large fragmentation of strength, in particular for the deeply bound $\nu f_{7/2}$ single-particle state. In the ^{55}Sc$\rightarrow$^{54}Sc reaction the $\nu f_{7/2}$ strength is situated completely above the neutron separation energy and thus does not contribute to the measured one-neutron knockout cross-section, since the measurement of this cross-section relies on the survival of the residual nucleus.

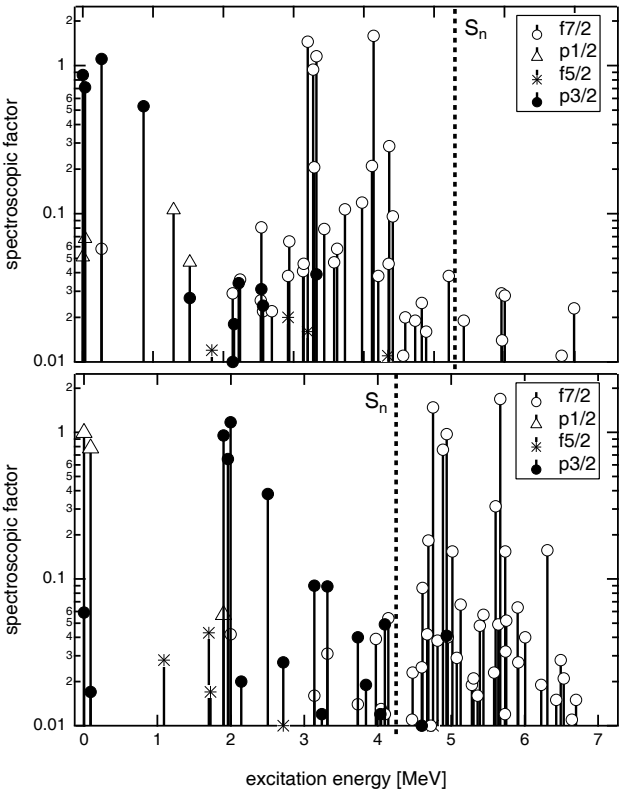

Fig. 8. Spectroscopic factors calcualted with the GXPF1A interaction of all possible states for ^{53}Sc $\rightarrow$ ^{52}Sc (top), and ^{55}Sc $\rightarrow$ ^{54}Sc (bottom). The positions of the neutron separation energies S_n in the residual nuclei at 5.2 and 4.2 MeV, respectively, are indicated by dashed lines.

The trends observed for the experimental cross-sections generally show very similar features, however, with some peculiar differences. The experimental $L = 1$ cross-sections also show the almost linear rise up to $N_{res} = 32$ and lie above the theoretical predictions. At $N_{res} = 33$ the $L = 1$ cross-section levels off or even drops. For the $L = 3$ cross-sections a more or less constant cross-section is observed from $N_{res} = 29$ to $N_{res} = 32$ while at $N_{res} = 33$ the $L = 3$ contribution drops basically to zero. The striking discrepancy between experiment and theory is the fact that the measured $L = 3$ cross-section is about a factor of two smaller than the theoretical prediction below $N_{res} = 32$ while the $L = 1$ cross-section is about 30–40% larger than predicted.

At the same time the measured inclusive cross-sections, plotted in fig. 9, compare well with the theoretical cross-sections if 75% of the full single-particle strength is used, in line with reductions observed in other direct reactions [40,43,44]. For ^{54}Sc$\rightarrow$^{53}Sc and ^{55}Sc$\rightarrow$^{54}Sc the theoretical inclusive cross-section is very sensitive to the exact position of the neutron separation energies in ^{53}Sc and ^{54}Sc, which systematics determine with accuracies of 355 keV and 585 keV, respectively [45].

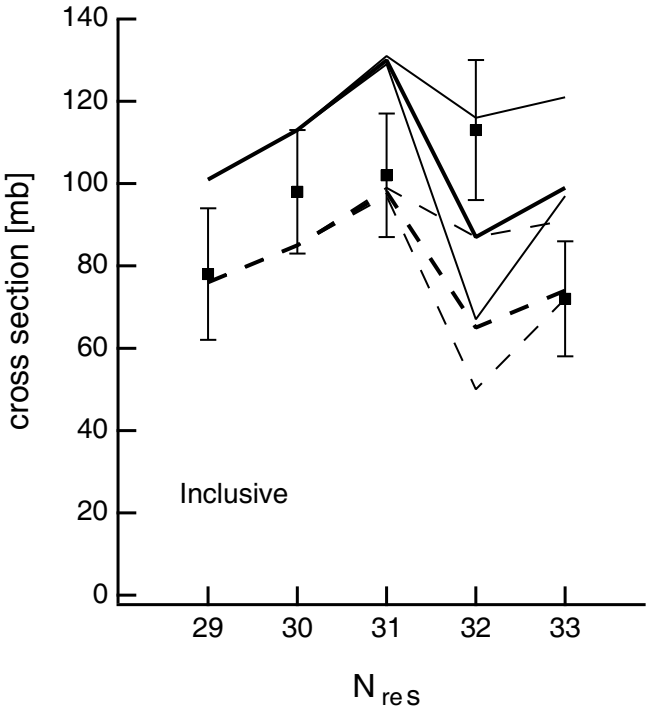

Fig. 9. Comparison of inclusive experimental (squares) and theoretical knockout cross-sections as a function of neutron number of the knockout residue. The theoretical cross-sections are shown for the full spectroscopic factors from the SM calculations up to the AME2011 [45] S_n value (solid line) and reduced by a factor 0.75 (dashed line). The lighter solid and dashed lines indicate the respective changes to the inclusive cross-sections due to the uncertainties of the neutron separation energies.

Taking into account this reduced single-particle strength, one has to compare the experimental cross-sections in fig. 7 to the dash-dotted lines. This improves the situation slightly for the $\nu f_{7/2}$ orbital but increases the discrepancy for the p-orbitals. One may consider that the reduced $L = 3$ cross-section could be due to a larger than predicted fragmentation of the $\nu f_{7/2}$ strength where some of the strength is pushed above the neutron separation energy. However, this scenario would not account for the larger than predicted $L = 1$ cross-sections.

It should also be noted that based on data from transfer experiments for ^{48}Ca and ^{49}Ti one may expect $\nu s_{1/2}$ and $\nu d_{3/2}$ hole states about 2.5 MeV above the $\nu f_{7/2}$ hole states. In ^{50,51}Sc these sd-fragments could be present at energies as low as 5.5 and 6.5 MeV, respectively, and thus below the respective neutron separation energies of 6.057(15) MeV and 6.752(25) MeV. Calculations show that contributions of up to 25 mb to the inclusive ^{51}Sc$\rightarrow^{50}$Sc cross-section could be expected if sd-shell strength comparable to that for ^{48}Ca($SF(1d_{3/2}) = 2.5$, $SF(2s_{1/2}) = 1.4$) is assumed to lie below $S_n(^{50}$Sc). While the measured inclusive cross-sections are in good agreement with the expectation for knockout from the pf-shell a small sd-shell contribution cannot be excluded for these two nuclei. In the heavier nuclei the sd-hole states will be situated well above the neutron separation energy.

However, the measured momentum distributions set some limits on the sd-shell contributions. We calculate that the linear combination of sd-shell states, as given above, located near the ^{50}Sc threshold, produce an essentially identical momentum distribution to that for the fitted linear combination of $L = 1$ and $L = 3$ states, and hence the data. So, the momentum distribution of the ^{51}Sc $\rightarrow$ ^{50}Sc knockout can be equally well described with only $L = 1$ ($\sigma_{L=1} = 54$ mb) and $L = 3$ ($\sigma_{L=3} = 24$ mb) momentum distributions, or by using a small contribution of $L = 0$ and $L = 2$ knockout ($\sigma_{sd} = 18$ mb) and somewhat reduced $L = 1$ ($\sigma_{L=1} = 42$ mb) and $L = 3$ ($\sigma_{L=3} = 18$ mb) contributions. This would reduce the under-prediction for the $L = 1$ cross-section somewhat but increase the over-prediction of the $L = 3$ cross-section. However, the coincident shapes of the sd- and pf-shell momentum distributions means that, even in the presence of such an sd-shell contribution, the deduced fractional contributions from $L = 1$ and $L = 3$ remain essentially unchanged.

This discrepancy between experiment and theory is most obvious for $N_{res} = 29$ where the experimental ratio of $(L = 1)$ to $(L = 3)$ strength is $3.9(6)/2.4(4) = 1.6 \pm \frac{0.6}{0.4}$ compared to the GXPF1A value of $1.94/7.42 = 0.26$. If the orbitals are filled in sequential order, $(f_{7/2})^8(p_{3/2})^2$ gives the ratio of 2/8 that is close to that obtained with GXPF1A for the states in ^{51}Sc below the neutron separation energy. Recent calculations by Holt *et al.* [33] using realistic low-momentum interactions V_{lowk} obtained by evolving a chiral N3LO NN potential predict that the energy of the neutron $p_{3/2}$ orbital drops when going from $N = 28$ to $N = 34$, effectively eliminating the $N = 28$ shell gap for ^{54}Ca (see fig. 1 of ref. [33]). If $N = 30$ had a pure $(f_{7/2})^6(p_{3/2})^4$ configuration the ratio of $(L = 1)$ to $(L = 3)$ strength is 4/6. Calculations with GXPF1A with a reduced $f_{7/2} - p_{3/2}$ gap of two MeV give $2.32/7.11 = 0.33$, still far from experiment. In addition, the spectrum for ^{51}Sc obtained with this reduced gap has a level density that is much higher than experiment. Thus, the large discrepancy around $N_{res} = 29$–31 between the experimental and expected ratio remains to be understood.

7 Summary

In summary, we have performed a relativistic knockout experiment on $^{51-55}$Sc using the GSI FRS as a two-stage magnetic spectrometer. Inclusive cross-sections and longitudinal momentum distributions were measured, allowing for the determination of the contributions of $L = 1$ and $L = 3$ knockout due to the removal of a neutron from the pf-shell orbitals as a function of neutron number. Comparison to shell model calculations using the GXPF1A residual interaction shows reasonable agreement concerning the increase of the $L = 1$ knockout cross-section with increasing neutron number as expected for a subsequent filling of the $\nu p_{3/2}$ and $\nu p_{1/2}$ neutron orbitals. The overall $L = 1$ knockout cross-section is slightly larger than the predicted value. At the same time a significantly lower $L = 3$ knockout cross-section was observed for the knockout from the $\nu f_{7/2}$ orbital compared to the theoretical predictions.

This mismatch in the cross-sections suggests that appreciable neutron $f_{7/2}$ spectroscopic strength has migrated across the $N = 28$ shell gap in this region. It is interesting to note that calculations with realistic nucleon-nucleon interactions plus three-body interactions [33] predict a reduction of the $N = 28$ shell gap in the respective Ca isotones, which could lead to such a migration

We acknowledge the excellent work of the GSI accelerator group. This work was supported by the BMBF under contracts 06MT238 and 06MT9156, by the DFG cluster of excellence *Origin and Structure of the Universe* (`http://www.universe-cluster.de`) and by the European Commission within the Sixth Framework Programme through I3-EURONS (contract no. RII3-CT-2004-506065). JAT acknowledges support from the United Kingdom Science and Technology Facilities Council (STFC) under Grant No. ST/J000051.

References

1. O. Sorlin, M.-G. Porquet, Prog. Part. Nucl. Phys. **61**, 602 (2008).
2. R. Krücken, Contemp. Phys. **52**, 101 (2011).
3. T. Otsuka, T. Suzuki, R. Fujimoto, H. Grawe, Y. Akaishi, Phys. Rev. Lett. **95**, 232502 (2005).
4. T. Otsuka, T. Matsuo, D. Abe, Phys. Rev. Lett. **97**, 162501 (2006).
5. T. Otsuka T. Suzuki, M. Honma, Y. Utsuno, N. Tsunoda, K. Tsukiyama, M. Hjorth-Jensen, Phys. Rev. Lett. **104**, 012501 (2010).
6. T. Otsuka, T. Suzuki, J.D. Holt, A. Schwenk, Y. Akaishi, Phys. Rev. Lett. **105**, 032501 (2010).
7. R. Kanungo *et al.*, Phys. Rev. Lett. **102**, 152501 (2009).
8. C. R. Hoffman *et al.*, Phys. Lett. B **672**, 17 (2009).
9. T. Otsuka, R. Fujimoto, Y. Utsuno, B.A. Brown, M. Honma, T. Mizusaki, Phys. Rev. Lett. **87**, 082502 (2001).
10. M. Honma, T. Otsuka, B.A. Brown, T. Mizusaki, Phys. Rev. C **65**, 061301 (2002).
11. M. Honma, T. Otsuka, B.A. Brown, T. Mizusaki, Phys. Rev. C **69**, 034335 (2004).
12. E.K. Warburton *et al.*, Phys. Rev. C **41**, 1147 (1990).
13. A. Poves *et al.*, Nucl. Phys. A **694**, 157 (2001).
14. E. Caurier *et al.*, Eur. Phys. J. A **15**, 145 (2002).
15. A. Poves, F. Nowacki, E. Caurier, Phys. Rev. C **72**, 047302 (2005).
16. S. Bhattacharyya *et al.*, Phys. Rev. C **79**, 014313 (2009).
17. T.R. Rodríguez, J.L. Egido, Phys. Rev. Lett. **99**, 062501 (2007).
18. J.I. Prisciandaro *et al.*, Phys. Lett. B **510**, 17 (2001).
19. R.V.F. Janssens *et al.*, Phys. Lett. B **546**, 55 (2002).
20. P.F. Mantica *et al.*, Phys. Rev. C **67**, 014311 (2003).
21. S.N. Liddick *et al.*, Phys. Rev. C **70**, 064303 (2004).
22. B. Fornal *et al.*, Phys. Rev. C **70**, 064304 (2004).
23. D.-C. Dinca *et al.*, Phys. Rev. C **71**, 041302(R) (2005).
24. B. Fornal *et al.*, Phys. Rev. C **72**, 044315 (2005).
25. A. Bürger *et al.*, Phys. Lett. B **622**, 29 (2005).
26. A. Gade *et al.*, Phys. Rev. C **73**, 037309 (2006).
27. A. Gade *et al.*, Phys. Rev. C **74**, 021302(R) (2006).
28. A. Gade *et al.*, Phys. Rev. C **74**, 047302 (2006).
29. S. Zhu *et al.*, Phys. Lett. B **650**, 135 (2007).
30. P. Mantica *et al.*, Phys. Rev. C **77**, 014313 (2008).
31. S. Zhu *et al.*, Phys. Rev. C **80**, 024318 (2009).
32. P. Maierbeck *et al.*, Phys. Lett. B **675**, 22 (2009).
33. J.D. Holt *et al.*, J. Phys. G **39**, 085111 (2012).
34. A.T. Gallant *et al.*, Phys. Rev. Lett. **109**, 032506 (2012).
35. H. Geissel *et al.*, Nucl. Instrum. Methods B **70**, 286 (1992).
36. B. Sitar *et al.*, Nucl. Instrum. Methods A **419**, 503 (1998).
37. J. Eberth *et al.*, Progr. Part. Nucl. Phys. **46**, 389 (2001).
38. N. Iwasa *et al.*, Nucl. Instrum. Methods B **126**, 284 (1997).
39. H. Weick, private communication.
40. P.G. Hansen, J.A. Tostevin, Annu. Rev. Nucl. Part. Sci. **53**, 219 (2003).
41. B.A. Brown, Phys. Rev. C **58**, 220 (1998).
42. L. Ray, Phys. Rev. C **20**, 1857 (1979).
43. A. Gade *et al.*, Phys. Rev. C **77**, 044306 (2008).
44. B.A. Brown, P.G. Hansen, B.M. Sherrill, J.A. Tostevin, Phys. Rev. C **65**, 061601(R) (2002).
45. Georges Audi, Wang Meng, private communication (2011).